Development and Interpretation of improved Nitrous Acid Retrievals (DINAR)

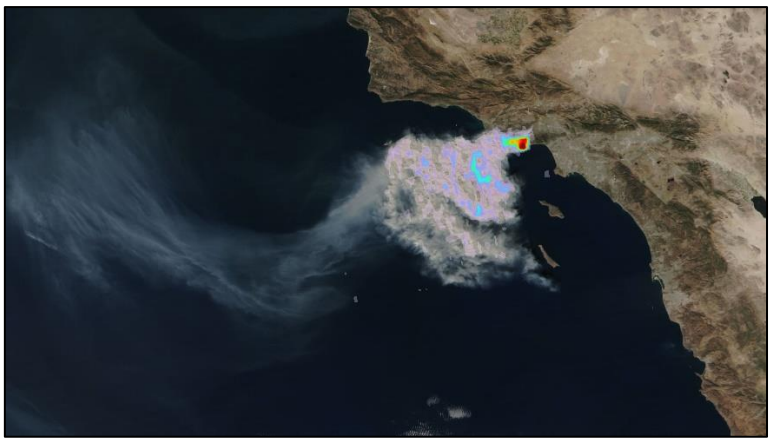

Algorithm Theoretical Baseline Document

document number	:	DINAR_HONO_ATBD
authors	:	Nicolas Theys, Huan Yu, Bruno Franco, Lieven Clarisse
Distributed to	:	Christian Retscher
issue	:	2.0
date	:	2024-02-05
status	:	Final

Table of Contents

1 Introduction

Nitrous acid (HONO) is a precursor of the hydroxyl radical in the atmosphere, which controls the degradation of greenhouse gases, contributes to photochemical smog and ozone production, and influences air quality. Understanding the sources and sinks of HONO in the atmosphere is therefore important for advancing our knowledge in atmospheric chemistry. However, measurements of HONO are sparse and have been mostly limited to laboratory experiments, remote-sensing or in-situ measurements from ground-based or aircraft platforms. Recently, there has been a growing effort to detect HONO from satellite measurements.

The Development and Interpretation of improved Nitrous Acid Retrievals (DINAR) project (see http://hono.aeronomie.be), funded by ESA, supports the algorithmic development of HONO retrievals from space, its validation as well as the interpretation of the results using a modeling framework. The purpose of this document is to give a description of the algorithms, and to discuss the necessary input and auxiliary data, and the output that will be generated. A brief description of the error estimates associated to the retrievals is also provided.

2 Satellite instruments

DINAR aims at developing HONO products from complementary satellite payloads including polar-orbiting and geostationary platforms, operating in the ultraviolet-visible and thermal infrared spectral ranges. Here we give a short description of the instruments that will be used to generate the project output datasets.

TROPOMI

The TROPOspheric Monitoring Instrument (TROPOMI), is the single-payload of the Sentinel-5 Precursor (S-5P) platform launched in October 2017. It is an atmospheric mission with a dedicated focus on the tropospheric composition (Veefkind et al., 2012). TROPOMI is a nadir-viewing remote sensing instrument measuring the solar radiation reflected by the Earth and backscattered by its atmosphere. The instrument is a push-broom imaging spectrometer covering ultraviolet to shortwave infrared wavelengths with a spectral resolution of 0.25–1 nm. Flying in a low-Earth early afternoon polar orbit with a wide swath of 2600 km resulting in daily global coverage, it delivers vertically integrated abundances of key atmospheric constituents (O_3, NO_2, SO_2, HCHO, CHOCHO, CO, CH_4) complemented by cloud and aerosol information.

The footprint on the ground of the satellite measurement depends mainly on the across-track position in the swath and on the spectral band. For HONO, the ultraviolet spectral band 3 is used, and the swath is divided into 450 across-track positions (also referred to as 'rows'). The spatial resolution for the center of the swath is approximately 3.5 x 7 km² (across-track x along-track) until 6 August 2019 when the sampling improved to 3.5 x 5.5 km².

GEMS

The Geostationary Environment Monitoring Spectrometer (GEMS) was launched on February 28, 2022, onboard the Geostationary Korea Multi-Purpose Satellite 2 (GEO-KOMPSAT-2B). GEMS is the first geostationary UV-visible instrument dedicated to monitor key atmospheric constituents (O_3, NO_2, SO_2, HCHO, CHOCHO and aerosols), at hourly resolution (Kim et al., 2020). GEMS is an imaging spectrometer with a spectral coverage from 300 to 500 nm, a resolution of ~0.6 nm and a high signal to noise ratio. GEMS observes the Asia domain at latitudes of 5°S to 45°N and longitudes of 75°S to 145°E more than eight times a day. We make use of L1b radiance data provided by NIER at the original spatial resolution of ~3.5 × 8 km² (ORI files). GEMS is divided into 2,048 north (N)–south (S) spatial pixels and scans from east (E) to west (W) in 695 steps.

IASI

The Infrared Atmospheric Sounding Interferometer (IASI) is an infrared Fourier transform spectrometer developed jointly by CNES (the French space agency) and EUMETSAT. IASI is mounted on-board the European polar-orbiting Metop satellite with the primary objective to improve numerical weather predictions, by measuring tropospheric temperature and humidity with high horizontal resolution and sampling, with 1 km vertical resolution, and with respectively 1 K and 10% accuracy (Camy-Peyret and Eyre, 1998). As a second priority, IASI contributes to atmospheric composition measurements for climate and chemistry applications (Clerbaux et al., 2009). IASI measures the infrared radiation of the Earth's surface and atmosphere between 645 and 2760 cm^{-1} at nadir and along a 2200 km swath perpendicular to the satellite track. A total of 120 views are collected over the swath, divided as 30 arrays of 4 individual Field-of-views (FOVs) varying in size from 6 × 6 × π km² at nadir (circular 12 km diameter pixel) to 10 × 20 × π km² at the larger viewing angle (ellipse-shaped FOV). IASI offers global coverage twice daily, with overpass times at around 9:30 am and pm, local solar time. The good spatial and temporal sampling of IASI is complemented by fairly high spectral and radiometric performances: the calibrated level 1C radiances are at 0.5 cm^{-1} apodized spectral resolution (the instrument achieves a 2 cm optical path difference), with an apodized noise that ranges below 2500 cm^{-1}

between 0.1 and 0.2 K of a reference blackbody at 280 K (Hilton et al., 2011). The following IASI Metop year ranges have been used in the analysis: IASI/Metop-A (2007-2021), IASI/Metop-B (2013-ongoing), IASI/Metop-C (2019-ongoing).

3 Algorithm description

3.1 Satellite UV-visible measurements

3.1.1 State of the art

In the UV-visible, there is only one study about observations of HONO from space. Using TROPOMI measurements, Theys et al. (2020) presented the first satellite mapping of HONO at the global scale, covering one year of data. This study demonstrated the capability of high spatial resolution nadir UV-visible instruments to sense HONO in freshly emitted fire plumes, over different ecosystem type. HONO slant column densities (SCD) were retrieved from TROPOMI radiance spectra using the Differential Optical Absorption Spectroscopy (DOAS) method (Platt and Stutz, 2008). Nitrogen dioxide (NO_2) SCDs, co-retrieved in the same wavelength range, were used to estimate enhancement ratios of the measured HONO SCD to the NO_2 SCD (RHN), as a proxy of the photochemical production rate of HONO. This pioneering study has advanced our understanding of global fire HONO emissions in that current emission inventories (i.e., emission factors) were too low. Moreover, model simulations have shown that the observed HONO level accounts for two-thirds of the total OH production in fire plumes, so that HONO appears as the main driver of the downwind plume chemistry. This suggest that pyrogenic HONO emissions can have a substantial impact on atmospheric composition, which enhances regional ozone levels.

Starting from the HONO DOAS retrievals, the algorithm described below aims at (1) improving the spectral fitting of HONO, (2) better isolating the HONO detections from the retrieved SCDs, and (3) work towards a quantitative HONO product (vertical columns).

3.1.2 Algorithm overview

Determination of the vertical column density (VCD, vertically integrated concentration) of HONO is obtained in two steps. First, the measured top-of-atmosphere radiances are analyzed and yield the slant columns (SCD, or the integrated concentration along the light path). In a second step, a radiative transfer calculation of air mass factors (AMF) is performed to convert the SCD into the VCD output (VCD=SCD/AMF). A diagram illustrating the algorithm modules is given in Figure 1.

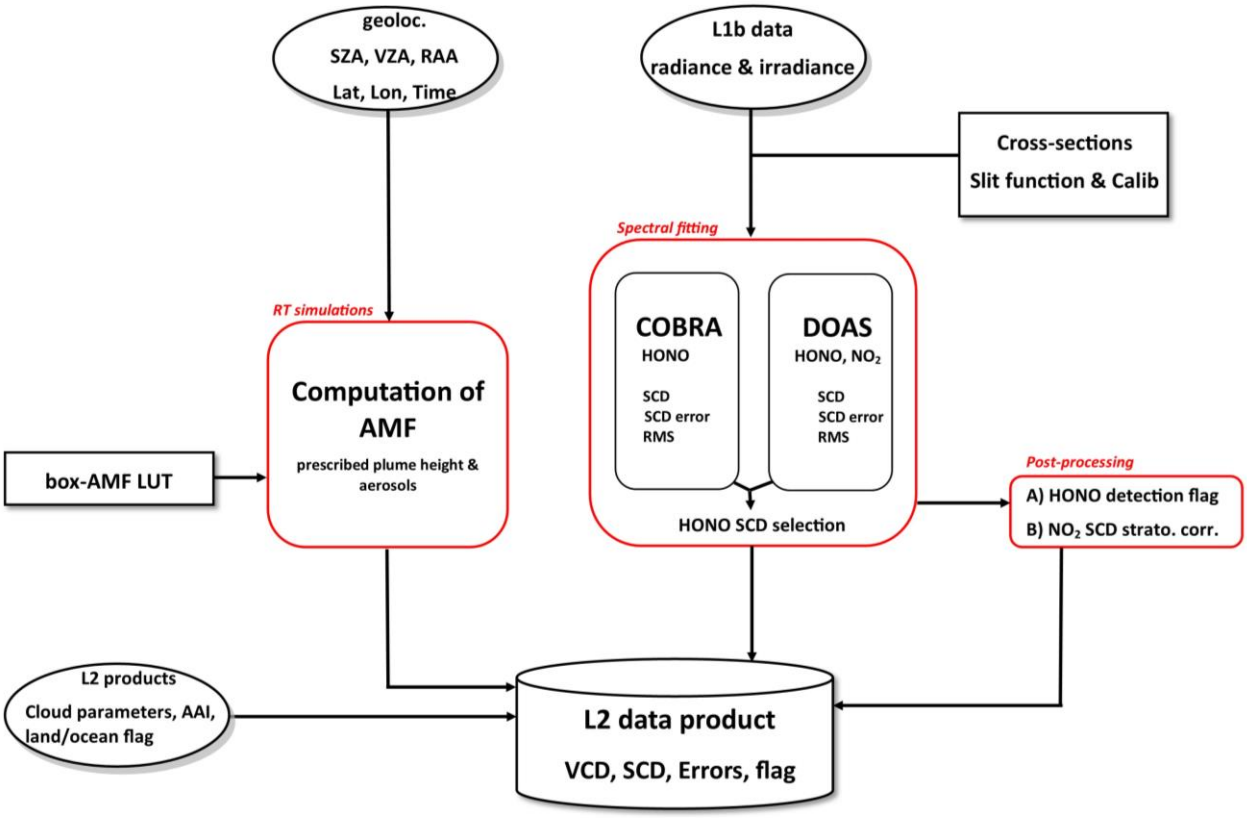

Figure 1: Flow diagram of the HONO UV-visible retrieval algorithm.

The radiance and irradiance data are read from the L1b files, along with geolocation data as pixel coordinates and observation geometry. The relevant absorption cross section data as well as characteristics of the instrument like slit function and wavelength calibration parameters are used as input of the spectral fitting module. The HONO fit is performed using two different approaches - the COBRA and DOAS – and a selection of the final HONO SCD is performed. The DOAS sub-module is also used to retrieve NO2 SCD in the same UV spectral range. In a post-processing step, the results from the spectral fitting module are used to design A) a HONO detection flag and B) a stratospheric NO2 SCD correction. The latter is useful to estimate enhancement ratio of HONO SCD relative to NO2 SCD (see Theys et al., 2020). Subsequently, the slant column is converted to a vertical column through division by an air mass factor which accounts for the average light path through the atmosphere. The AMF is computed for prescribed HONO plume heights and aerosols, and altitude-resolved air mass factors extracted from a pre-computed look-up-table. This look up table has been created using the VLIDORTv2.7 radiative transfer model (Spurr, 2006) at a single wavelength representative for the retrieval interval (i.e., 355 nm). Finally, several variables are read from operational L2 products (cloud parameters, Absorbing

Aerosol Index, etc) and copied in the L2 HONO product, as these are useful to inform on clouds and aerosols for each measurement.

The next subsections give details on the two algorithmic steps (spectral fitting and radiative transfer calculations), as well as an overview of the input data needed for the retrievals.

Spectral fitting

The main algorithm module for the retrieval of HONO SCDs is based on the Covariance-Based Retrieval Algorithm (COBRA). Inspired by previous work in the thermal infrared (Walker et al., 2011), it has been successfully adapted to the UV retrieval of SO2 from TROPOMI (Theys et al., 2021).

In a preparatory step, we compute the total measured optical depth $y = -\log(I/I_0)$, which is the logarithmic ratio of the wavelength calibrated measured intensity (I) and the solar intensity spectrum (I_0). For the wavelength calibration, we use the same approach as for the operational SO2 algorithm (as described in Theys et al., 2017). The optical depth spectrum y is then extracted over the wavelength range 337-375 nm, an interval where HONO has distinct absorption spectral features (see Fig. 2).

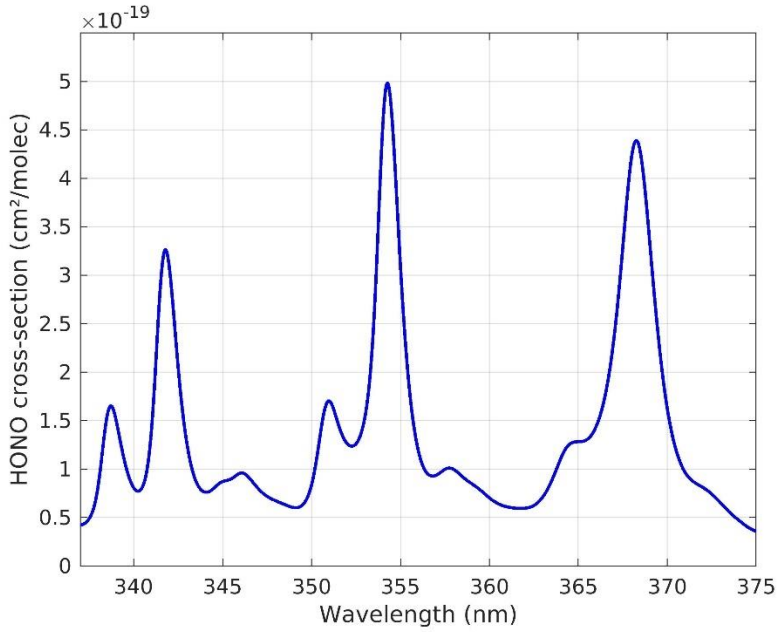

Figure 2: Nitrous acid cross-section (from Stutz et al., 2000) in the UV range 337-375 nm convolved at the TROPOMI resolution.

We assume the measurement vector (y) can be linearized around a background HONO-free spectrum $\bar{y}$:

$$y = \bar{y} + k.SCD + \epsilon_{bg} + \epsilon \quad (1)$$

with ϵ_{bg} being the uncertainty on the HONO-free spectrum, and ϵ is the measurement noise. The HONO contribution to the measured spectral optical depth is the product of the instrument slit convolved absorption cross-section vector k (an example is given in Fig2, for the TROPOMI row #225) and the HONO slant column density *SCD* (in molecules/cm²).
The basic principle of the method is to consider all contributions to the difference $(y - \bar{y})$ other than HONO as an error term $(\epsilon_{bg} + \epsilon)$ with a Gaussian distribution. If one can define an ensemble Y of N measured spectra, representative of the total $(\epsilon_{bg} + \epsilon)$ variability, and characterized by a mean measurement vector $\bar{y}$ and a covariance matrix S:

$$S = \frac{1}{N-1} \cdot \sum_{i=1}^{N} (y_i - \bar{y})(y_i - \bar{y})^T \quad (2)$$

then the solution of the problem writes as:

$$\widehat{SCD} = (k^T S^{-1} k)^{-1} k^T S^{-1} (y - \bar{y}) \quad (3)$$

It follows that the error on the retrieved SCD is given by:

$$\widehat{SCD}_{err} = \sqrt{(k^T S^{-1} k)^{-1}} \quad (4)$$

Fundamentally, COBRA generalizes the measurement error covariance matrix used in Optimal Estimation Methods (OEM; Rodgers, 2000) by incorporating geophysical background spectral variability (including all cross-correlations), variability from the atmosphere or induced by instrumental changes. A remarkable feature of COBRA is its simplicity. The SCD retrieval in Eq. 3 reduces to a simple dot product between the $y - \bar{y}$ residue and $k^T S^{-1}$ (skipping the normalization factor $(k^T S^{-1} k)^{-1}$). Note also that the target SCD is only the fit parameter; this is contrast to most other retrieval methods.

However, the practical implementation for COBRA requires some caution. The main difficulty lies in the definition of the ensemble Y used to construct S (and $\bar{y}$). The reader is referred to Theys et al. (2021) for more detailed discussion on COBRA pro and cons. For the retrieval of HONO from TROPOMI, we have conducted several tests and come to the following implementation choices (the settings for GEMS are similar): the input spectra for the covariance matrix calculation are analyzed separately for each TROPOMI row. We also treat each orbit individually to account best for the orbit-to-orbit variability. The data are first screened for solar zenith angles larger than 65°, and to cope with the latitudinal dependence, the data are divided into 3 equal and non-overlapping along-track segments. For each segment, an initial covariance matrix S is derived and initial estimates of HONO SCDs are inverted through equation 3. In a second step, improved estimates of S and HONO SCDs are obtained iteratively by removing HONO contaminated spectra from the ensemble Y. To do this, we use the ratio of the SCD to its retrieval uncertainty (Eqs. 3 and 4), referred to as the signal to noise ratio (SNR):

$$SNR = \frac{k^T S^{-1}.(y-\bar{y})}{\sqrt{k^T S^{-1} k}} \quad (5)$$

A fixed SNR upper value of 3 is used for the filtering and the number of iterations is set to 3. Note that most pixels are HONO-free so the retrieved SCDs at first iteration are actually very close to the final SCDs, except in some rare cases of extended HONO plume. Finally, to evaluate the fit quality, we compute (and store in the files) the normalized root-mean-square χ with:

$$\chi^2 = \frac{1}{N-1}.(\Delta y^T S^{-1} \Delta y) \quad (6)$$

where $\Delta y = y - \bar{y} - k.\widehat{SCD}$ (residual) and N being the number of wavelengths in the fitting interval. This variable is typically close to 1, except for conditions of bad fit quality (χ>>1).

Compared to the initial DOAS results of Theys et al. (2020), the COBRA HONO SCDs display low noise (typically a reduction by a factor of 2-3). This is a direct result of the COBRA approach in that the wavelengths with the largest background radiance variability will have the lowest weights on the retrieved SCD (Eq. 3). Also, very small biases are observed in the COBRA data. However, in the spectral fitting module, it was decided to include a simplified DOAS sub-module. There are two reasons for this: (1) for the study of biomass burning plumes, it is important to retrieve NO2 SCDs (in the same spectral range as HONO), to compute the RHN, and for this, COBRA is not applicable, (2) in some cases, the DOAS HONO SCDs are believed to be more accurate than the COBRA HONO SCDs (see below).

For the DOAS module, we used the linearized form of the inversion problem:

$$y = K\,.x + \epsilon \quad (7)$$

where K is the forward model matrix with absorption cross-sections and other spectra, x is the state vector including SCDs of relevant trace gases and closure fit parameters and ϵ is the measurement noise (as in Eq. 1). The solution is obtained by simple least-square fitting:

$$\hat{x} = (K^T K)^{-1} K^T y \quad (8)$$

The DOAS settings used are summarized in Table1; these are nearly identical to the initial settings of Theys et al. (2020).

Table 1: Linear DOAS settings used for retrievals of HONO and NO_2 SCDs.

HONO and NO_2	Retrievals performed separately for each row
Fitting interval	337-375 nm
Cross-sections	HONO 296K (Stutz et al., 2000), NO_2 294K (Vandaele et al., 1998), water vapor (Polyansky et al., 2018), O_2-O_2 293K (Thalman and Volkamer, 2013), O_3 223K and 243K (Serdyuchenko et al., 2014), BrO 223K (Fleischmann et al., 2004), HCHO 298K (Meller and Moortgat, 2000), Ring (Chance and Spurr, 1997)
Polynomial	5th order
Intensity offset	Linear, 1st order
Wavelength shift, squeeze	Linear (Beirle et al., 2013)
Reference spectrum	Daily measured irradiance
Post-processing	NO_2 SCD stratospheric correction: Latitudinal parameterization (per across-track position) in clean Pacific sector (160°E-150°W)

From the analysis of the data, it turns out that the HONO SCDs from COBRA and DOAS agree well on average, for COBRA SCDs<10^{16} molecules/cm². As the HONO SCDs from COBRA are generally of better quality (lower noise and reduced noise), these are being used by default as final SCD product. However, for large COBRA SCDs >10^{16} molecules/cm², we observe sometimes significantly larger DOAS HONO SCDs (see Figure 3) and if the difference DOAS minus COBRA is larger than 2 x 10^{15} molecules/cm², we consider the DOAS HONO SCDs instead of the COBRA results. This choice is motivated by the fact that, in extreme conditions, the covariance matrix S will have difficulties to represent the observed conditions and spectral interferences with other trace gases present in the plume (e.g., HCHO, NO2) needs to be properly accounted for. By doing so, this merged product combines the advantages of both algorithms (improved sensitivity and good accuracy for large columns).

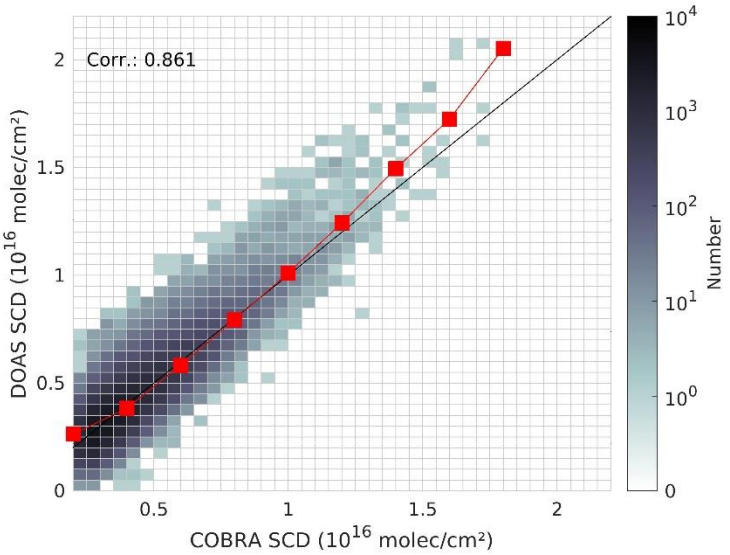

Figure 3: Comparison of HONO SCD from the COBRA and DOAS schemes for the period May 2018 to December 2022. The red squares are DOAS averaged SCDs for COBRA SCD bins. A good agreement is observed between both retrievals, except for large columns (COBRA SCD>1e16) where DOAS exhibits large values.

An example of HONO SCDs retrieved by TROPOMI is shown in Figure 4.

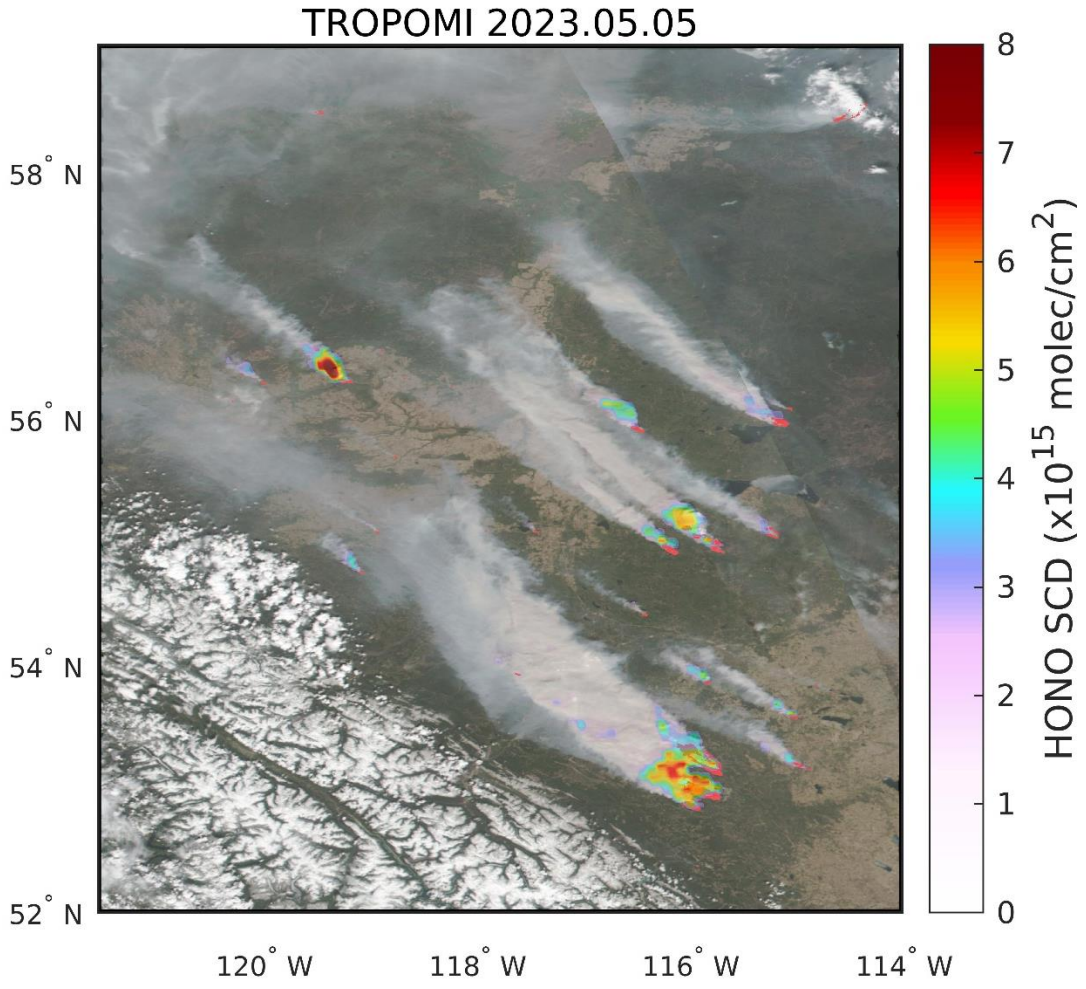

Figure 4: Example map of TROPOMI HONO SCDs for wildfires in Alberta, Canada, on 05 May 2023. The background layer is from the VIIRS/Suomi-NPP instrument (https://worldview.earthdata.nasa.gov/), which shows smoke aerosols and the fire source locations.

Finally, to increase and facilitate the usage of the HONO SCD data, a detection flag is constructed based on the retrieved HONO SCDs and SCD errors. The flag is based on the signal-to-noise ratio (defined in Eq.5). If the SNR of a pixel and the SNRs of at least 2 surrounding pixels are above a certain threshold, then the detection is considered as statistically significant, and the flag is activated. The flag assigning is as follows:

- **3**: high confidence (SNR>16)

- **2**: good confidence (SNR>8)
- **1**: reasonable confidence (SNR>4) if other data (e.g., AAI, fire radiative power) indicate presence of fires.
- **0**: no detection

We note that this flag is quite conservative and that other selection criteria are possible depending on the conditions or regions. The reader is invited to read the product readme file document for more information or to contact the main author of the present document.

Radiative transfer calculations.

The AMF simulates the trace gas concentration integrated along the complex photon path in the plume, relative to the vertical path. Here, the AMF can be formulated (Palmer et al., 2001) by:

$$AMF = \int bAMF(z).N(z).dz \quad (9)$$

where N(z) is the trace gas normalized concentration profile and bAMF is the height-resolved AMF (referred as box-AMF) that contains all dependences to parameters (wavelength, geometry, surface reflectance, clouds, aerosols, etc.) influencing the vertical sensitivity of the measurement, except N(z).

As a result of its short atmospheric lifetime, HONO is mostly detected near the fire sources (see Fig.4) where large amounts of smoke aerosols are present. Therefore, the measurement sensitivity can be strongly affected by aerosols, depending on the aerosol optical properties and extinction vertical profile. To study this effect, a set of AMFs were calculated at a wavelength of 355 nm for typical biomass burning plumes (as in Theys et al. 2020). Because HONO and aerosols are co-emitted, their vertical profiles were assumed to have the same shape modelled by a Gaussian peaking at 2km above the surface, with full width at half maximum of 0.5km (other cases with plume heights at 5km and 12km have also been simulated). Biomass burning aerosols were represented by a bi-modal log-normal particles size distribution (Wang et al., 2012), with a single scattering albedo between 0.75 and 0.95, indicative of fresh to aged aerosols. Figure 5 shows an example of the dependence of the AMFs with aerosol optical depths (AOD) and single scattering albedo (SSA). It illustrates the expected change in measurement sensitivity due to aerosols and the strong dependence on the aerosol parameters.

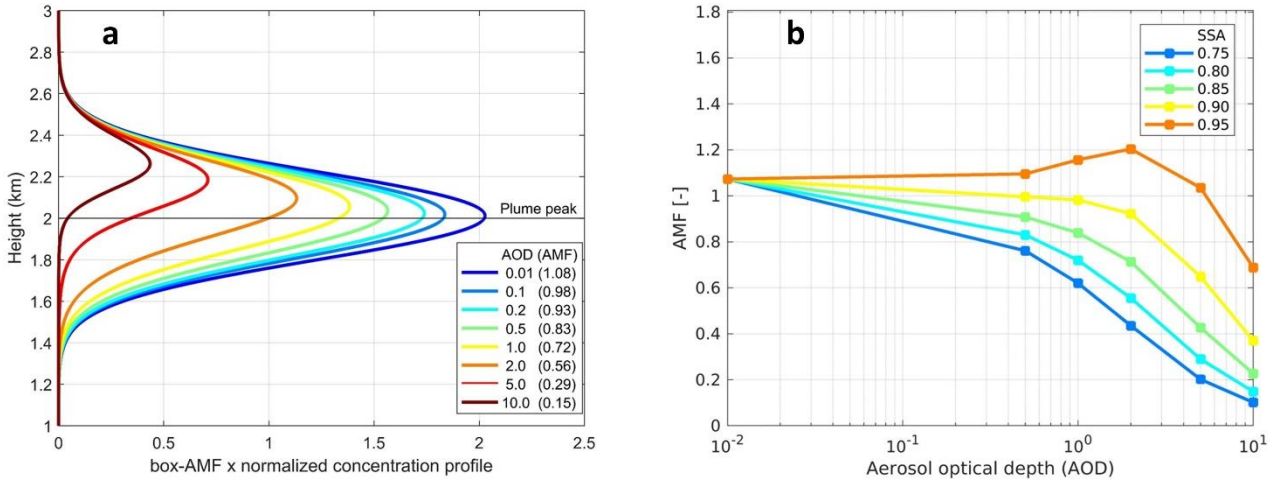

Figure5: Illustration of measurement sensitivity change for varying aerosol optical depth for a smoke plume peaking at 2km. (left) Height-resolved contribution to the total AMF for satellite nadir viewing geometry, as function of AOD. Calculations are for clear-sky standard atmosphere, 30° solar zenith angle, 0.05 surface albedo, and typical fresh biomass burning absorbing aerosols with SSA of 0.8. (right) Total AMFs as a function of AOD for the same conditions, with SSA varying between 0.75 and 0.95.

From these simulations, it is clear that a general AMF computation applicable globally is difficult because crucial parameters are poorly known, notably the trace gases vertical distribution and the aerosol optical properties and extinction vertical profile (impacting bAMF). Importantly, it turns out that the existing satellite UV-based aerosol algorithms have limitations to provide reliable information on aerosols parameters (AOD, SSA, aerosol height) for optically thick plumes (AOD>5).

As a workaround, the baseline for the HONO VCD product is to calculate air mass factors for each pixel (i.e., accounting for the observational geometry), but for a set of prescribed aerosol parameters and plume heights. The idea is that a wide range of conditions would be covered by the AMFs, and a user could easily infer (i.e., interpolate) an HONO VCD based on third party information (in terms of AOD, SSA, plume heights). This would allow also to calculate a VCD error due to uncertainties on the input parameters.

Overview of input data needed

The table below gives an overview of the data used as input of the algorithm.

Table 2 List of input data needed for generating the UV HONO VCD product.

Parameter	Physical unit	Source
Cross-sections	$cm^2.molec^{-1}$, except O2-O2 ($cm^5.molec^{-2}$) and Ring (1)	See table 1
Slit function	1	CKD (instrument specific)
Box-AMF look-up-table	1	Generated internally
Radiance	$mol\ s^{-1}\ m^{-2}\ nm^{-1}\ sr^{-1}$	L1b radiance product
Irradiance	$mol\ s^{-1}\ m^{-2}\ nm^{-1}$	L1b irradiance product
Latitude center and corners	degree	L1b radiance product
Longitude center and corners	degree	L1b radiance product
Time	degree	L1b radiance product
Solar zenith angle	degree	L1b radiance product
Viewing zenith angle	degree	L1b radiance product
Solar azimuth angle	degree	L1b radiance product
Viewing azimuth angle	degree	L1b radiance product
A priori HONO vertical profile shape	1	Prescribed, Gaussian function with plume height peaks (at 2, 5, 12 km a.g.l.) and 0.5 km FHWM
Aerosol extinction profile	km^{-1}	Same profile shape as HONO with a scaling to AOD= 1, 2, 5, 10
Single scattering albedo	1	Prescribed values of 0.7, 0.8, 0.9
Phase function	1	Prescribed (Wang et al., 2012)

3.1.3 Error estimates

The total retrieval uncertainty on the HONO vertical columns can be derived by propagation of errors from the two retrieval steps:

$$\sigma_{VCD}^2 = (\frac{\sigma_{SCD}}{AMF})^2 + (VCD.\frac{\sigma_{AMF}}{AMF})^2 \quad (10)$$

where $\sigma_{VCD}, \sigma_{SCD}, \sigma_{AMF}$ are the errors on the vertical column, slant column and air mass factor, respectively.

Completely characterizing the different error sources is difficult, as it depends very much on the observation conditions and on information on aerosols and plume height which are not easily available. For HONO and NO2 retrievals in the UV, SCD errors are relatively small. The SCD errors from the fits (mostly random errors) are of ~ 0.4

and 2 x 10^{15} molecules/cm^2, for HONO and NO2 respectively. The SCD systematic errors are typically of 10-15% (see supplementary material of Theys et al., 2020). Conversely, the AMF errors can be very large and are also difficult to assess. Comparison with other HONO measurements suggest that the error budget is dominated by uncertainty in the radiative transfer. For further details, the reader is referred to the DINAR validation report.

As described above, the AMF depends on many parameters, and the error on the AMF can be broken down into a squared sum of terms:

$$\sigma_{AMF}^2 = \sum_i \left(\frac{\partial AMF}{\partial var_i} . \sigma_{var_i}\right)^2 \quad (11)$$

where σ_{var_i} is the uncertainty on the ith variable var_i (AOD, SSA, plume height, etc.) and $\frac{\partial AMF}{\partial var_i}$ is the sensitivity of the AMF to a change in var_i(Jacobean). In principle, the partial derivates could be estimated from the set of AMFs calculated by the HONO VCD algorithm, and a user could calculate an AMF error for realistic values of uncertainties σ_{var_i}, through Eq. 11.

3.2 Satellite thermal infrared measurements

3.2.1 State of the art

The capacity to detect and measure HONO using thermal infrared (TIR) satellite sensors has been relatively restricted until now. In 2011, Clarisse et al. (2011) reported the first detection of HONO in a nadir satellite observation, specifically from IASI/Metop-A, within a pyrocumulus cloud during the "Black Saturday" bushfires that engulfed the Victoria State, Australia, in February 2009. The spectral signature of HONO was highlighted through a synthetic reconstruction of the IASI spectrum with a radiative transfer model using the optimal estimation (OE) technique. A decade later, De Longueville et al. (2021) implemented an enhanced technique for the detection of weak absorbers (whitening transformation) and once more identified HONO in IASI spectra, this time captured within a large fire plume originating from the extensive bushfires that ravaged Southeast Australia in 2019/2020. Shortly after, Dufour et al. (2022) used an OE approach to carry out the first TIR retrieval of HONO concentrations in the same Australian fire plume, based on observations from IASI and the Cross-track Infrared Sounder (CrIS) embarked on the Suomi National Polar-orbiting Partnership (S-NPP) satellite. As a result, HONO has exclusively been detected using TIR satellite sounders within the 2009 and 2019/2020 Australian fires, which exhibited excellent conditions (e.g., substantial emissions and intense convection) for the retrieval of reactive species from spaceborne observations.

In the next subsections, we describe an enhanced approach for the detection and retrieval of HONO from IASI observations in biomass burning plumes.

3.2.2 Algorithm overview

The detection and retrieval of HONO from IASI spectra relies on the Artificial Neural Network for IASI (ANNI) general framework version 4, initially developed for the retrieval of ammonia (NH_3) and volatile organic compounds (e.g., Clarisse et al., 2023; Franco et al., 2018). A schematic overview of ANNI v4 is presented in Fig. 6. The actual calculation of the columns relies on two computational steps: (1) The calculation for each IASI observation of a hyperspectral range index (HRI). This quantity is a very sensitive, broadband spectral index that quantifies the signal strength of a target absorber in a radiance spectrum. (2) The conversion of the HRI into a total column abundance via an artificial feedforward neural network (NN).

In addition to the HRI, the NN relies on a series of auxiliary parameters related to the state of the atmosphere and surface. Perturbations to the input data of the NN allows quantification of the uncertainties associated with single-pixel retrieved columns. Appropriate filtering of the data (before and after the retrieval) removes cloudy scenes and observations with limited or no sensitivity to the target trace gas.

While the retrieval itself is simple and fast, the initial setup (blue boxes in Fig. 6) of the HRI and NN is nontrivial. In particular, both rely on weight constants that must be determined with care beforehand from a data set of real (for the HRI) and synthetic (for the NN) IASI spectra.

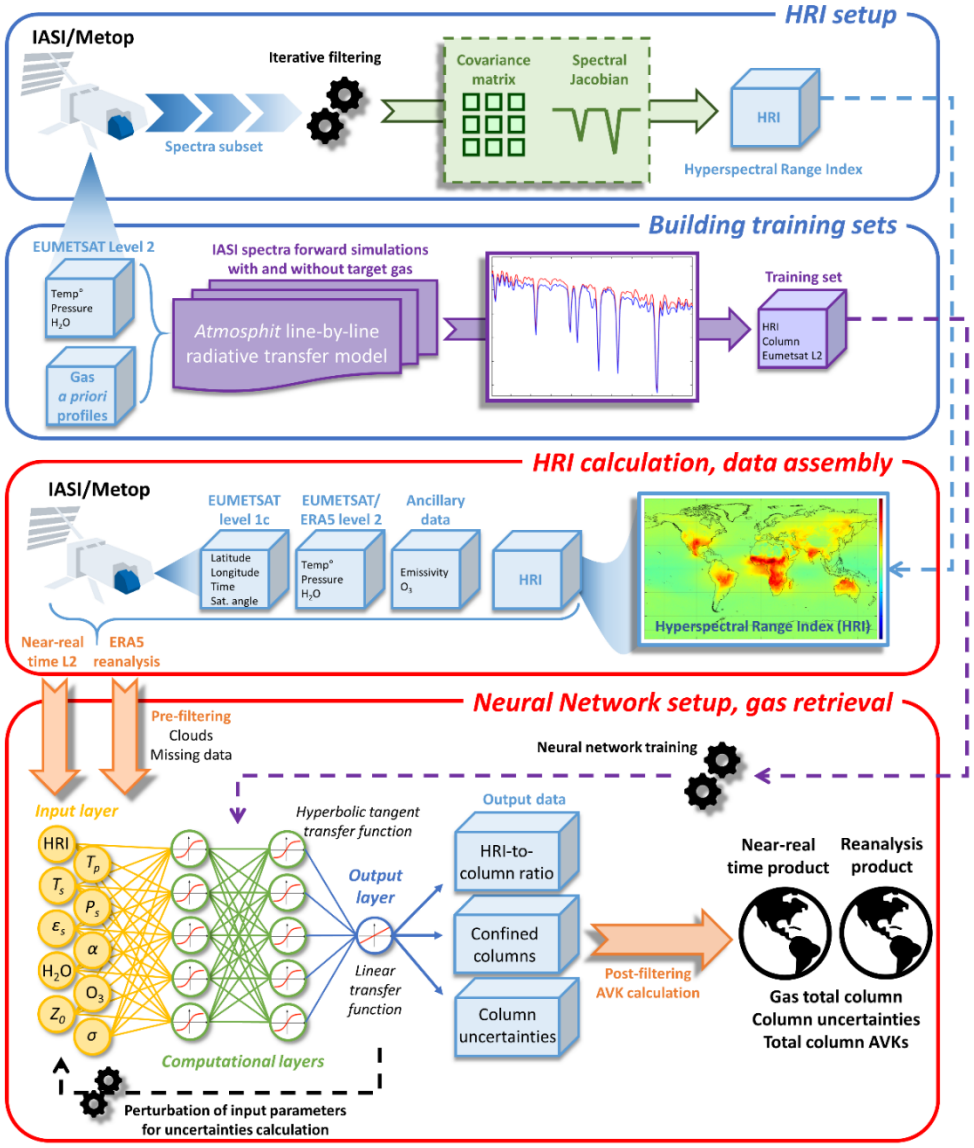

Figure 6: Conceptual flowchart of the ANNI v4 retrieval method of trace gases (adapted from Franco et al., 2018)

Spectral fitting

Proposed by Walker et al. (2011), the HRI is a dimensionless index that quantifies the strength of the spectral signature of a target gas in an observed spectrum y:

$$\mathrm{HRI} = \frac{K^T S_{\bar{y}}^{-1}(y-\bar{y})}{\sqrt{K^T S_{\bar{y}}^{-1} K}} \frac{1}{N} \quad (11)$$

where K is a spectral Jacobian, S_y a covariance matrix, and $\bar{y}$ the mean spectrum generated from a representative data set of background spectra associated with a climatological column of the target gas, and N an extra normalization factor (see further). The HRI is normalized to have a mean of zero and a standard deviation of one when calculated on the data set of background spectra. The HRI is particularly suitable for the detection of highly variable infrared absorbers, like HONO, which are not observed in every spectrum. In this case, the climatological column amount is close to zero and the background spectra are those without observable signature of HONO. The HRI can encompass spectral ranges of up to several hundred cm^{-1} to exploit all the channels in which the target species absorbs. This results in a substantial gain of sensitivity over other detection methods and makes it highly suitable for the detection of broadband absorption features (Clarisse et al., 2013).

Larger spectral ranges lead in principle to a more sensitive HRI. However, this is true only in the linear regime in which the covariance matrix describes a normal distribution. In practice, it can be advantageous to exclude spectral ranges where nonlinearity prevails. In addition, it might be useful to avoid a spectral interval in which another species with a similar spectral signature is absorbing. For HONO, the range was set to 1210-1305 cm^{-1} that exploits the Q-branch of its ν_3 band at 1263 cm^{-1}. The wide spectral range was chosen to minimize interferences with surface emissivity features. This band has been preferred over the ν_4 bands HONO (Q-branches at 790 and 852 cm^{-1}) because the 1210-1305 cm^{-1} range is less affected by interferences and has a significantly lower measurement noise in the IASI spectrum (Clerbaux et al., 2009). The Jacobian K is the derivative of the radiance spectrum with respect to the column abundance of the target species, and this was generated by the line-by-line radiative transfer model Atmosphit (Coheur et al., 2005) for a standard atmosphere.

For each target species, the HRI calculation also depends on a generalized covariance matrix S_y and an associated background spectrum $\bar{y}$. S_y determines the weight of each spectral channel, and ideally expresses the variability and covariance of all interfering species, but explicitly not that of the target species (Walker et al., 2011). Such a matrix can be obtained from a representative set of IASI spectra with a constant, climatological column amount of the target species. For short-lived trace gases like HONO, the pair (S_y, $\bar{y}$) can be constructed from spectra with no observable signature of the gas (the associated climatological column is then close to zero). To select such spectra, an iterative approach is usually followed (Clarisse et al., 2013). First, a representative set of IASI spectra is built, consisting of all the spectra from the 15th of each month of 2013, but sampled to yield a spatially uniform distribution (to avoid over-representing polar regions). This entire set is then used for the generation of a first (S_y, $\bar{y}$) pair. This allows the production of a first set of HRI, which in turn was used to remove the spectra with detectable signatures of the trace gas (typically HRI > 3;

see below). The reduced set of spectra allows the calculation of a better (S_y, $\bar{y}$) pair. Repeating this process several times leads to convergence of the set of spectra, of the corresponding (S_y, $\bar{y}$), and of the HRI. As the initial normalization of the HRI is not preserved in the iterative process, an additional normalization factor (N) is needed in equation (11), which is recalculated at each iteration as the standard deviation of the HRI over a remote ocean area with no observable amount of the target species.

For HONO, however, as its detection is highly challenging, almost all the spectra from the initial set have no detectable signature of HONO, which leaves too few spectra for calculating a representative (S_y, $\bar{y}$) pair through this iterative process. Therefore, no iteration was performed for HONO and only the first generated (S_y, $\bar{y}$) pair was used. Moreover, observations over selected desert regions (e.g., the Saharan and Arabian deserts) were added to the set of IASI spectra, as no HONO is expected for those, and to make the HRI more robust for the surface emissivity features found over deserts.

The covariance matrix S_y can be decomposed into a set of orthogonal vectors s_i and their corresponding eigenvalues λ_i representing the variance along each vector:

$$S_y = \sum_{i=1}^{n} \lambda_i s_i s_i^T \quad (12)$$

Typically, there is a domain of eigenvalues consisting of a few very small λ_i with a negligible contribution to the HRI. However, Clarisse et al. (2023) explained recently that changes in instrument calibration or post-processing can affect the contribution of these λ_i in the spectra, resulting in significant alterations in the HRI (e.g., biases between the IASI instruments and discontinuities in the time series). Excluding such small λ_i from the covariance matrix S_y mitigates most of these alterations. For HONO, we determined that the seven smallest eigenvalues λ_i needed to be excluded.

After regularization of S_y, minor residual positive trends were still observed in the time series of HONO HRI over remote oceanic regions: 4×10^{-5} per day for IASI-A after 2011, and 1.1×10^{-4} per day for IASI-B and -C. These trends were subsequently removed from the HRI time series. Furthermore, after detrending, a monthly climatology of HONO HRI was built and subtracted from the final set of HONO HRI to eliminate parts of the surface emissivity that affects the HONO absorption band in the IASI spectra.

A typical example of HONO detection in fresh biomass burning plumes, using the HRI, is presented in Fig. 7 for wildfires in Spain/Portugal in October 2017.

Despite the previous corrections, the HONO HRI is still prone to anomalies and false detections due to the weak, broadband spectral absorption of HONO and the presence of other absorbers overlapping the HONO signature. To extract the IASI data with significant HONO enhancements in fire plumes, a specific filter was created, which partly relies on the co-detection of HONO with NH_3 and ethylene (C_2H_4) within the same IASI spectrum. Both NH_3 and C_2H_4 are short-lived fire tracers routinely retrieved from IASI observations with ANNI (Van Damme et al., 2021; Franco et al., 2022) and

are much less affected by spectral anomalies. An HONO enhancement is considered as a genuine detection of pyrogenic HONO if the following conditions are met:

- am observations: $HRI_{HONO}>8$ or ($HRI_{HONO}>4$ and ($HRI_{NH3}>50$ or $HRI_{C2H4}>4$))
- pm observations: $HRI_{HONO}>8$ or ($HRI_{HONO}>4$ and ($HRI_{NH3}>12$ or $HRI_{C2H4}>4$))

This filter often restricts HONO detection to instances where NH_3 and C_2H_4 are also detectable. However, this cautious approach aims to minimize false positives, and the number of genuine HONO enhancements mistakenly filtered out is minimal. NH_3 thresholds are set high to prevent false HONO detections in areas with elevated NH_3 backgrounds, such as those resulting from agriculture (Van Damme et al., 2018).

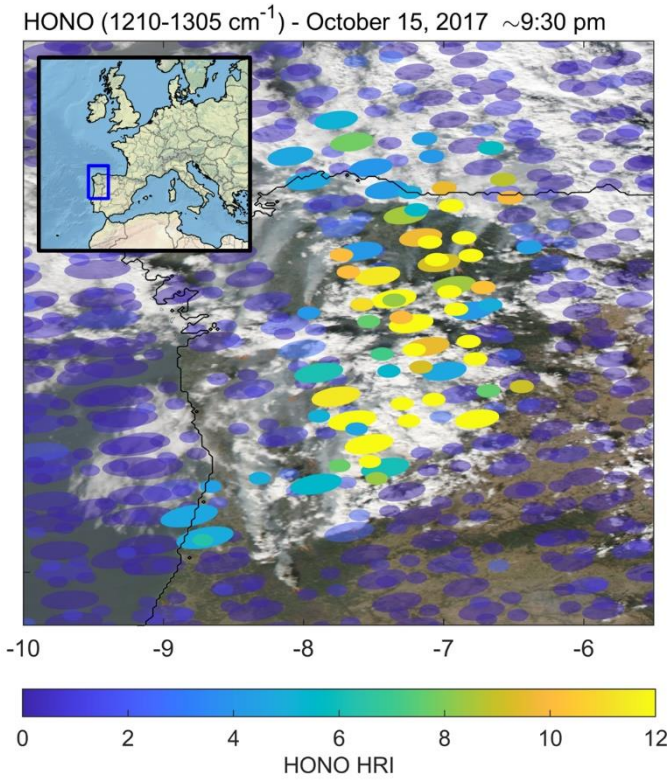

Figure 7: HONO HRI from single IASI/Metop-A and -B nighttime overpasses (~9.30 pm) over wildfires in Spain/Portugal on October 15, 2017. The shape of each dot corresponds to the footprint on ground of an individual IASI measurement. Base map is from MODIS/Aqua visible imagery (~1:30 pm).

Radiative transfer calculations.

The spectral signature (HRI) of a target gas is a complex function of the species abundance and of all the other parameters entering into the radiative transfer, such as

the state of the atmosphere and surface, interfering species, and the viewing angle. The main idea of the ANNI retrieval approach is to use a NN to approximate the complex inverse function that maps the HRI and the auxiliary parameters to a column abundance. A NN consists of interconnected nodes (small mathematical functions) organized in layers, as illustrated in Fig. 6. The weights of the nodes are trained to best fit the complex analytical relationships that bind any set of input variables feeding the NN to the corresponding output variable. NNs learn from the presentation of examples, and so training sets are required consisting of matching input (auxiliary parameters, column abundance) and output data (spectrum and associated HRI).

The performance of a NN depends largely on the quality of the training set, which should be as comprehensive and representative as possible. This means that the set should cover a large range not only of the column abundances of the target gas (and associated HRI) but also of the auxiliary parameters. Each IASI observation (L1C radiance spectra) is distributed with corresponding Level 2 data consisting of a temperature, pressure, H_2O profile, and surface temperature (August et al., 2012). These were used here as input for the auxiliary parameters of the training data set. We selected approximately 500,000 IASI L2 data over the year 2013, regularly sampled in space and time to ensure a comprehensive and representative data set. Hence, it contains a very large range of atmospheric conditions (e.g., surface temperature from 220 to 330 K), which are representative for all possible scenes one can encounter in the whole IASI dataset (including other years).

As the surface temperature and emissivity vary more over land than over oceans, 66 % of the data were chosen to be associated with land observations. Additional data were added for the higher and lower thermal contrasts (TCs; temperature difference between the surface and the air layer located just above) to ensure that extreme TCs (between -30 and 40 K) are sufficiently represented within the training data set. Finally, a random column of the target gas was associated with each sample in the data set. These columns were generated by randomly scaling a vertical profile of the gas (see below) from $<1\times10^{14}$ to $>1\times10^{17}$ molecules cm^{-2}. IASI spectra were simulated for each sample in this data set using Atmosphit. Due to small remaining forward model errors, HRI values produced by Atmosphit can be biased. For this reason, a spectrum was simulated for each sample with and without the target species. The HRI of the simulation without the target gas was then used to offset the HRI of the other simulation, in such a way that an HRI value of zero always corresponds to the absence of the trace gas. Note that since Atmosphit does not simulate the clouds, the resulting training data set is cloud-free.

As discussed in Whitburn et al. (2016), the vertical profile of the target gas used in the forward simulations was parameterized with a Gaussian function as:

$$\mathrm{vmr}_{(\mathrm{HONO})} = k \times e^{-\frac{(z-z_0)^2}{2\sigma^2}} \quad (13)$$

The peak height (z_o) indicates the altitude where most HONO is concentrated, corresponding to the height of the fire plume. The standard deviation (σ) describes the thickness of the HONO layer. To ensure the NN's reliability across various fire plume conditions, we conducted forward simulations with varied parameters: z_o from the surface to 20 km, and σ between 0.1 and 3 km. The scaling factor (k in ppb) was adjusted at z_o to control the abundance of HONO in the forward simulations.

It is advantageous to keep the size of the NN as small as possible by only considering the parameters that affect most the output variable. A satisfactory NN performance was achieved by training with the following input parameters:

- HRI
- temperature profile at 0, 0.5, 1, 1.5, 2, 2.5, 3, 5, 7, 10, 13, 16, 19, 25 and 30 km
- skin temperature
- surface pressure
- emissivity: average over selected channels in the atmospheric windows
- H_2O partial column profile between 0-1, 1-2, 2-3, 3-5, 5-7, 7-10 and 10-30 km
- satellite viewing angle
- peak HONO altitude (z_o)
- spread of the HONO profile (σ)

The HRI-to-column ratio was adopted as output of the NN instead of the gas column itself, as using the ratio allows (1) for a better training of the NN owing to its smaller dynamic scale and (2) to translate the instrumental noise—which is part of the HRI—in a linear way to the retrieved column (Whitburn et al., 2016; Van Damme et al., 2017). This guarantees that the retrieval on noisy HRI does not lead to a biased product. However, slightly negative columns can be retrieved because of this noise.

Based on the training performances, a NN that consists of two computational layers was set up with each 12 nodes. A multilayer NN is usually better at tackling nonlinearities than a many-node, single-layer NN. 2-D error plots summarize the performance of the NN on the training set in terms of relative error and biases as a function of gas total column and TC (Fig. 8). Normally distributed noise was added to all the input data to evaluate the performances as realistically as possible (right panels). The final NNs are seen to be practically unbiased for positive TCs. For the non-background gas abundance, the relative errors range from 10% to 50%, with the highest errors found for the low gas columns. The relative errors increase for lower background columns (top panels) where the columns approach the IASI detection threshold. However, the biases remain low (bottom panels). As can be expected, the NN does not perform well for observational scenes with low negative TCs.

The actual retrieval consists first of collecting the required input data, that is, the HRI of the observed spectrum and the matching auxiliary data. While some of the auxiliary data are directly taken from the IASI L1 and L2, the meteorological input variables are derived from the hourly European Center for Medium-Range Weather Forecasts

(ECMWF) ERA5 reanalysis (Hersbach et al., 2020), collocated with the corresponding IASI measurements. The ERA5 data enables more comprehensive and coherent retrievals across the IASI operational time series (Van Damme et al., 2021).

Following the ANNI procedure, z_o and σ are typically adjusted to represent gas emission patterns over land and low-altitude transport over the ocean. However, this approach is not suitable for HONO, as it is predominantly detected by IASI in elevated fire plumes. Instead, we determined the value of z_o based on a 1°×1° monthly climatology of fire plume altitudes derived from the Cloud-Aerosol Lidar and Infrared Pathfinder Satellite Observation (CALIPSO) 5-km Aerosol Layer products (Winker et al., 2009) over the 2006-2020 period. The same approach was applied for the retrieval of dust with ANNI (Clarisse et al., 2019). For the layer thickness, we considered a constant thin layer for HONO and set the value of σ at 350 m. Future developments of ANNI might consider to derive z_o and σ directly from the IASI observations.

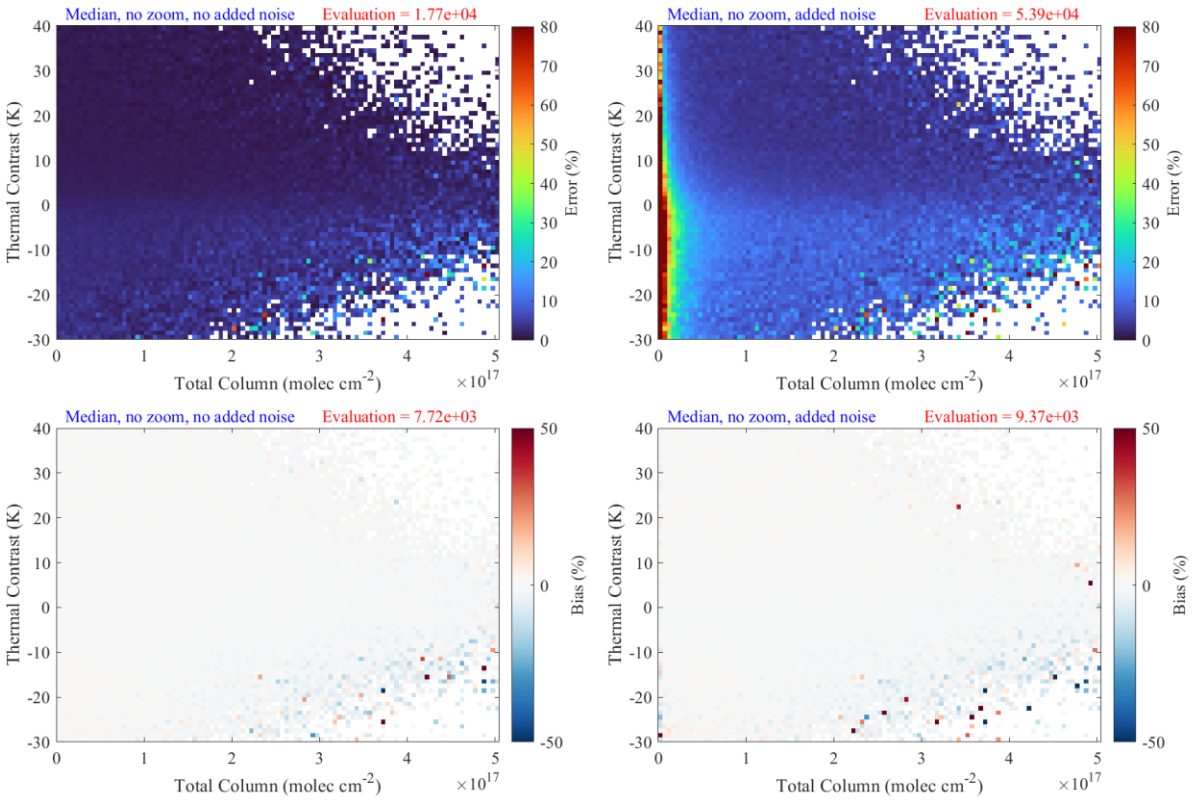

Figure 8: Performance evaluation (top: error, bottom: bias, both in %) of the NN, with and without adding noise. The median value is shown in each grid box, which removes the effect of outliers and allows assessing the real performance of the NN.

The NN is then fed with these data, as illustrated in Fig. 6. Finally, the inverse of the HRI-to-column ratio obtained as output of the NN is multiplied by the associated HRI, yielding the total column of the target gas. Before the NN is applied to the real IASI

measurements, all satellite observations with invalid L1 or L2 are filtered out. Moreover, for HONO, only the IASI measurements with a confirmed detection of pyrogenic HONO undergo the retrieval process.

A single pixel cloud flag associated with each retrieved HONO column is provided and can be used to distinguish IASI measurements based on the presence of residuals clouds and smoke (i.e., clear sky, <10% cloud coverage, between 10 and 25% cloud coverage, and >25% cloud coverage). The cloud flag is based on a NN trained with data from the official IASI L2 cloud product v6.5 (Whitburn et al., 2022).

An example of HONO total columns retrieved from IASI measurements in a fresh biomass burning plume is presented in Fig. 9. In this example, the dark blue, semi-transparent IASI pixels indicate measurements without confirmed HONO detections, which did not undergo the retrieval process.

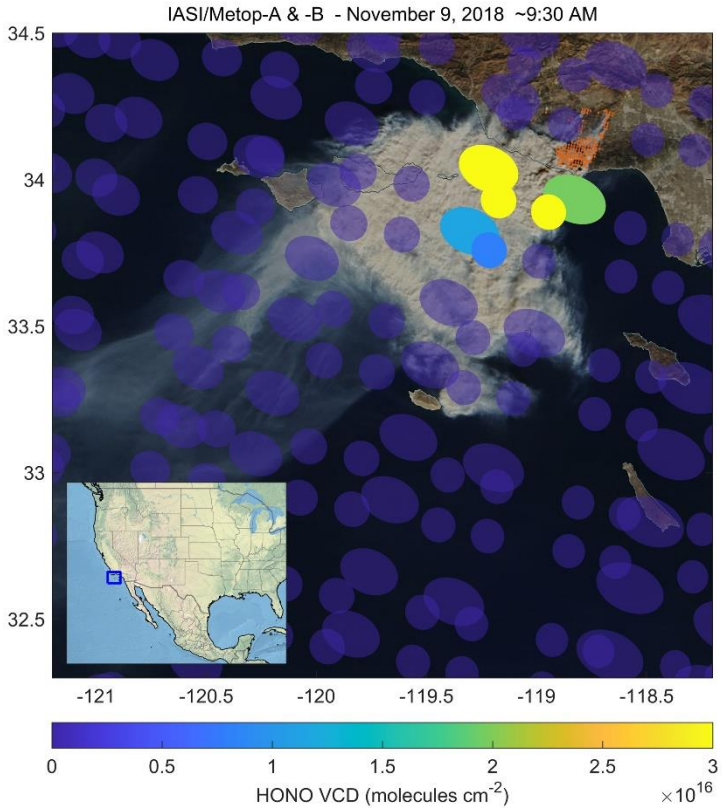

Figure 9: HONO vertical column densities (VCD) from IASI/Metop-A and -B (~9:30 am overpass) during the Woolsey Fire, California, on November 9, 2018. The shape of each IASI dot corresponds to the footprint on ground of an individual measurement. The small orange dots indicate actives fires detected by MODIS/Terra (~10:30 am). Base map is from MODIS/Terra visible imagery.

New in ANNI v4 is the calculation of a total column averaging kernel (AVK) vector associated with each retrieved column of the target gas, which allows accounting for the influence of the a priori profile shape when comparing IASI columns with independent data. The value of the AVK vector A_z^a at altitude z is determined as:

$$A_z^a = {\hat{X}^a}/{\hat{X}^z} \quad (14)$$

With $\hat{X}^a$ the estimate of the true gas total column, and $\hat{X}^z$ the retrieved column assuming that the target gas is confined within a narrow atmospheric layer at the altitude z. While $\hat{X}^a$ corresponds to the column retrieved using the standard parameters z_o and σ, as described earlier, $\hat{X}^z$ is retrieved assuming that $z_o = z$ and $\sigma =$ 100 m, and is successively calculated for 14 a priori profiles confined at different z ranging between 0 and 20 km (the NN was trained to retrieve the target gas for various (z, σ) pairs). All the details on the AVK formalism can be found in Clarisse et al. (2023). An example AVK for an HONO retrieval in British Columbia wildfires, Canada, is shown in Fig. 10.

Large differences between the CALIPSO climatology-based and true altitudes of the fire plume can occur, resulting in large biases on the assumed vertical distribution of HONO and on the retrieved columns $\hat{X}^a$. When studying a specific fire plume for which the altitude is known confidently from independent data, the single pixel "confined" columns $\hat{X}^z$ (provided as ANNI outputs) corresponding to that altitude layer can be used instead of $\hat{X}^a$ as a more realistic estimation of HONO's true vertical abundance.

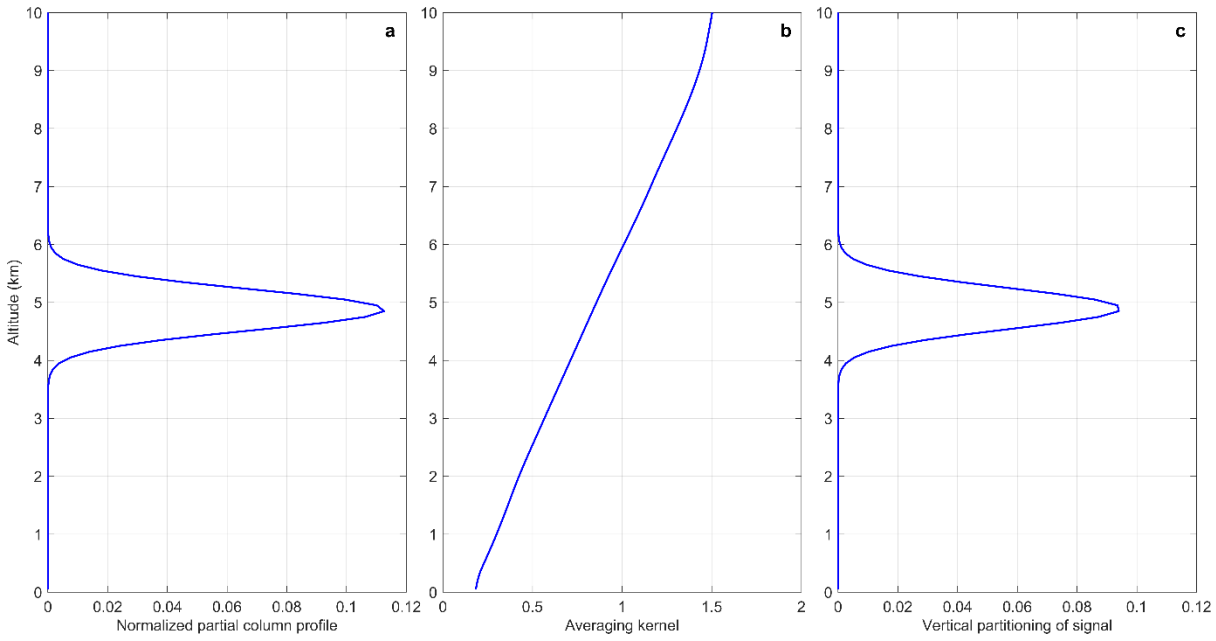

Figure 10: A priori vertical profile (**a**), averaging kernel **(b)**, and vertical partitioning of signal (**c**) of the retrieval of HONO from an IASI/Metop-A observation recorded in British Columbia wildfires, Canada, on August 17, 2018, ~9:30 pm.

Overview of input data needed

The input data required throughout the ANNI v4 process (i.e., HRI set up, construction of the training set, NN training, and retrieval) are listed in Table 3.

Parameter	Physical unit	Source
HONO cross-sections	$cm^2.molec^{-1}$	Sharpe et al. (2004)
HITRAN 2012 linelist	/	Rothman et al. (2013)
Radiance	$W\ m^{-2}\ sr^{-1}\ m$	IASI L1 product
Latitude center	degree	IASI L1 product
Longitude center	degree	IASI L1 product
Time	Dd HH:MM:SS	IASI L1 product
Solar zenith angle	degree	IASI L1 product
Viewing zenith angle	degree	IASI L1 product
Temperature profile	K	IASI L2 product and ERA5
Skin temperature	K	IASI L2 product and ERA5
Pressure profile	Pa	IASI L2 product
Surface pressure	Pa	IASI L2 product and ERA5
Ground height	km	NOAA TerrainBase Global Terrain Model https://www.ngdc.noaa.gov/mgg/gravity/1999/document/html/tbase.html
H_2O partial column profile	molecules cm^{-2}	IASI L2 product and ERA5
Surface emissivity over land	/	Prescribed, based on Zhou et al. (2011)
Surface emissivity over sea	/	Prescribed, based on Nalli et al. (2008)
Land sea mask	/	NOAA TerrainBase Global Terrain Model https://www.ngdc.noaa.gov/mgg/gravity/1999/document/html/tbase.html
A priori HONO vertical profile shape (15 levels)	Mol. mol^{-1}	Prescribed, Gaussian function with plume height between 0 and 20 km and spread between 0.1 and 3 km
HONO HRI	/	Calculated from IASI L1
NH_3 HRI	/	Calculated from IASI L1 (Clarisse et al., 2023)
C_2H_4 HRI	/	Calculated from IASI L1 (Franco et al., 2022)

Fire plume height	km	Prescribed, based on CALIPSO (Winker et al., 2009)
Cloud coverage	/	Prescribed, based on Whitburn et al. (2022)

3.2.3 Error estimates

In ANNI v4, the random $\sigma_{r\hat{X}}$ and systematic $\sigma_{s\hat{X}}$ uncertainties of the individual retrieved column $\hat{X}$ are reported separately, as described by Clarisse et al. (2023). Each of these uncertainties were estimated by propagating the uncertainties of the different input parameters (presented in Table 4) through the NN while considering the correlations that might exist between some of these uncertainties:

$$\sigma^2_{\hat{X}} = J^{\mathrm{T}} \mathrm{S}_p J \quad (15)$$

With S_p the error covariance matrix of the input parameters p_i (with covariances $S_{p,ij} = \sigma_{p_i p_j}$), and J the Jacobian of the retrieval with $\partial\hat{X}/\partial p_i$ as components. In practice, it was found that all the correlations between the different uncertainties can be neglected, except between the layers of the temperature profile. Therefore, in the block diagonal covariance matrix, a block diagonal was used for the elements corresponding to the temperature profile, and a diagonal for the other input parameters.

Note that uncertainty on the vertical profile is removed when applying the AVK. Consequently, uncertainties are calculated with and without the vertical profile uncertainty (Table 4). Random and systematic uncertainties can be combined, and an estimate of the total uncertainty on a retrieved column $\hat{X}$ can be obtained as:

$$\sigma^2_{\hat{X}} = \sigma^2_{r\hat{X}} + \sigma^2_{s\hat{X}} \quad (16)$$

Further details on the retrieval uncertainties are available in Clarisse et al. (2023).

Table 4: Estimated random and systematic uncertainties of the input parameters (reproduced from Clarisse et al., 2023).

Component	Random σ_r	Systematic σ_s
HRI	1	0.1 + 10%
Surface temperature (K)	1.5	0.5
Emissivity	0.01	0.005
Temperature profile, land (K)	1-2	0.5-1
Temperature profile, sea (K)	0.5-1	0.5-1
Surface pressure (Pa)	500	250
Water vapor profile	10-20%	5-10 %
HONO profile peak altitude (m)	800	400
HONO profile width (m)	200	100

4 References

August, T., Klaes, D., Schlüssel, P., Hultberg, T., Crapeau, M., Arriaga, A., O'Carroll, A., Coppens, D., Munro, R., & Calbet, X.: IASI on Metop-A: Operational Level 2 retrievals after five years in orbit. *J. Quant. Spectrosc. Radiat. Transf.* **113**, 1340–1371 (2012). https://doi.org/10.1016/j.jqsrt.2012.02.028

Beirle, S., Sihler, H., andWagner, T.: Linearisation of the effects of spectral shift and stretch in DOAS analysis, Atmos. Meas. Tech., 6, 661–675, https://doi.org/10.5194/amt-6-661-2013, 2013.

Camy-Peyret, C., & Eyre, J.: The IASI Science Plan. Technical report, A Report From The IASI Sounding Science Working Group (1998).

Chance, K., Spurr, R. J. Ring effect studies: Rayleigh scattering including molecular parameters for rotational Raman scattering, and the Fraunhofer spectrum. *Appl. Optics*. **36**, 5224–5230 (1997).

Clarisse, L., Clerbaux, C., Franco, B., Hadji-Lazaro, J., Whitburn, S., Kopp, A. K., Hurtmans, D., and Coheur, P.-F.: A Decadal Data Set of Global Atmospheric Dust Retrieved From IASI Satellite Measurements. *J. Geophys. Res. Atmos.* **124(3)**, 1618-1647 (2019). https://doi.org/10.1029/2018JD029701

Clarisse, L., Coheur, P.-F., Prata, F., Hadji-Lazaro, J., Hurtmans, D., and Clerbaux, C.: A unified approach to infrared aerosol remote sensing and type specification. *Atmos. Chem. Phys.* **13(4)**, 2195–2221 (2013). https://doi.org/10.5194/acp-13-2195-2013

Clarisse, L., Franco, B., Van Damme, M., Di Gioacchino, T., Hadji-Lazaro, J., Whitburn, S., Noppen, L., Hurtmans, D., Clerbaux, C., and Coheur, P.: The IASI NH3 version 4 product: averaging kernels and improved consistency. *Atmos. Meas. Tech. Discuss.* (2023). https://doi.org/10.5194/amt-2023-48

Clarisse, L., R'Honi, Y., Coheur, P.-F., Hurtmans, D., and Clerbaux, C.: Thermal infrared nadir observations of 24 atmospheric gases. Geophys. Res. Lett. **38(10)**, L10802 (2011). https://doi.org/10.1029/2011GL047271

Clerbaux, C., Boynard, A., Clarisse, L., George, M., Hadji-Lazaro, J., Herbin, H., Hurtmans, D., Pommier, M., Razavi, A., Turquety, S., Wespes, C., and Coheur, P.-F.: Monitoring of atmospheric composition using the thermal infrared IASI/MetOp sounder. *Atmos. Chem. Phys.* **9(16)**, 6041–6054 (2009). https://doi.org/10.5194/acp-9-6041-2009

Coheur, P.-F., Barret, B., Turquety, S., Hurtmans, D., Hadji-Lazaro, J., and Clerbaux, C.: Retrieval and characterization of ozone vertical profiles from a thermal infrared nadir sounder. *J. Geophys. Res.* **110**, D24303 (2005). https://doi.org/10.1029/2005JD005845

De Longueville, H., Clarisse, L., Whitburn, S., Franco, B., Bauduin, S., Clerbaux, C., Camy-Peyret, C., and Coheur, P.-F.: Identification of Short and Long-Lived Atmospheric Trace Gases From IASI Space Observations. *Geophys. Res. Lett.* **48(5)**, e2020GL091742 (2021). https://doi.org/10.1029/2020GL091742

Dufour, G., Eremenko, M., Siour, G., Sellitto, P., Cuesta, J., Perrin, A., and Beekmann, M.: 24 h Evolution of an Exceptional HONO Plume Emitted by the Record-Breaking 2019/2020 Australian Wildfire Tracked from Space. *Atmosphere* **13(9)**, 1485 (2022). https://doi.org/10.3390/atmos13091485

Fleischmann, O. C., Hartmann, M., Burrows, J.P., Orphal, J. New ultraviolet absorption cross-sections of BrO at atmospheric temperatures measured by time-windowing Fourier transform spectroscopy. *J. Photochem. Photobiol. A.* **168**, 117–132 (2004).

Franco, B., Clarisse, L., Stavrakou, T., Müller, J.-F., Van Damme, M., Whitburn, S., Hadji-Lazaro, J., Hurtmans, D., Taraborrelli, D., Clerbaux, C., and Coheur, P.-F.: A general framework for global retrievals of trace gases from IASI: Application to methanol, formic acid, and PAN. *J. Geophys. Res. Atmos.* **123**, 13,963–13,984 (2018). https://doi.org/10.1029/2018JD029633

Franco, B., Clarisse, L., Van Damme, M., Hadji-Lazaro, J., Clerbaux, C., and Coheur, P.-F.: Ethylene industrial emitters seen from space. *Nat. Comm.* **13(1)**, 6452 (2022). https://doi.org/10.1038/s41467-022-34098-8

Hilton, F., August, T., Barnet, C., Bouchard, A., Camy-Peyret, C., Clarisse, L., Clerbaux, C., Coheur, P.-F., Collard, A., Crevoisier, C., Dufour, G., Edwards, D., Faijan, F., Fourrié, N., Gambacorta, A., Gauguin, S., Guidard, V., Hurtmans, D., Illingworth, S.,

Jacquinet-Husson, N., Kerzenmacher, T., Klaes, D., Lavanant, L., Masiello, G., Matricardi, M., McNally, T., Newman, S., Pavelin, E., Péquignot, E., Phulpin, T., Remedios, J., Schlüssel, P., Serio, C., Strow, L., Taylor, J., Tobin, D., Uspensky, A., & Zhou, D.: Hyperspectral Earth Observation with IASI. *Bull. Am. Meteorol. Soc.* **93(3)**, 347-370 (2012). https://doi.org/10.1175/BAMS-D-11-00027.1

Kim, J. et al. New era of air quality monitoring from space: Geostationary Environment Monitoring Spectrometer (GEMS). *Bull. Am. Meteorol. Soc.* **101**, E1–E22 (2020).

Meller, R., Moortgat, G. K. Temperature dependence of the absorption cross section of HCHO between 223 and 323 K in the wavelength range 225–375 nm. *J. Geophys. Res.* **105**, 7089–7102 (2000).

Nalli, N., Minnett, P., and van Delst, P.: Emissivity and reflection model for calculating unpolarized isotropic water surface-leaving radiance in the infrared. I: Theoretical development and calculations. *Appl. Opt.* **47(21)**, 3701-3721 (2008). https://doi.org/10.1364/AO.47.003701

Palmer, P. I. et al. Air mass factor formulation for spectroscopic measurements from satellites: Application to formaldehyde retrievals from the Global Ozone Monitoring Experiment. *J. Geophys. Res.* **106**, 14539–14550 (2001).

Platt, U., and Stutz, J.: Differential Optical Absorption Spectroscopy (DOAS), Principle and Applications, ISBN 3-340-21193-4, Springer Verlag, Heidelberg, 2008.

Polyansky, O. L. et al. Exomol molecular line lists XXVI: a complete high accuracy line list for water. *Mon. Not. R. Astron. Soc.* **480**(2), 2597–2608 (2018).

Rodgers, C. D.: Inverse Methods for Atmospheric Sounding, Theory and Practice, World Scientific Publishing, Singapore-New-Jersey-London-Hong Kong, 2000.

Serdyuchenko, A., Gorshelev, V., Weber, M., Chehade, W., Burrows, J. P. High spectral resolution ozone absorption cross-sections – Part 2: Temperature dependence. *Atmos. Meas. Tech.* **7**, 625–636 (2014).

Rothman, L. S., Gordon, I. E., Babikov, Y., Barbe, A., Chris Benner, D., Bernath, P. F., Birk, M., Bizzocchi, L., Boudon, V., Brown, L. R., Campargue, A., Chance, K., Cohen, E. A., Coudert, L. H., Devi, V. M., Drouin, B. J., Fayt, A., Flaud, J.-M., Gamache, R. R., Harrison, J. J., Hartmann, J.-M., Hill, C., Hodges, J. T., Jacquemart, D., Jolly, A., Lamouroux, J., Le Roy, R. J., Li, G., Long, D. A., Lyulin, O. M., Mackie, C. J., Massie, S. T., Mikhailenko, S., Müller, H. S. P., Naumenko, O. V., Nikitin, A. V., Orphal, J., Perevalov, V., Perrin, A., Polovtseva, E. R., Richard, C., Smith, M. A. H., Starikova, E., Sung, K., Tashkun, S., Tennyson, J., Toon, G. C., Tyuterev, Vl. G., and Wagner, G.: The HITRAN2012 molecular spectroscopic database. *J. Quant. Spectrosc. Radiat. Transf.* **130**, 4-50 (2013). https://doi.org/10.1016/j.jqsrt.2013.07.002

Sharpe, S. W., Johnson, T. J., Sams, R. L., Chu, P. M., Rhoderick, G. C., and Johnson, P. A.: Gas-Phase Databases for Quantitative Infrared Spectroscopy. *Appl. Spectrosc.* **58(12)**, 1452-1461 (2004). https://doi.org/10.1366/0003702042641281

Spurr, R. J. VLIDORT: a linearized pseudo-spherical vector discrete ordinate radiative transfer code for forward model and retrieval studies in multilayer multiple scattering media. J. Quant. Spectrosc. Rad. 102, 316–342 (2006).

Stutz, J. et al. UV-vis Absorption Cross-Section of Nitrous Acid. *J. Geophys. Res.* **105**, 14585–14592 (2000).

Thalman, R. M., Volkamer, R. Temperature Dependent Absorption Cross-Sections of O_2-O_2 collision pairs be- tween 340 and 630nm and at atmospherically relevant pressure. *Phys. Chem. Chem. Phys.* **15**, 15371–15381 (2013).

Theys, N., De Smedt, I., Yu, H., Danckaert, T., van Gent, J., Hörmann, C., Wagner, T., Hedelt, P., Bauer, H., Romahn, F., Pedergnana, M., Loyola, D. and Van Roozendael, M.: Sulfur dioxide retrievals from TROPOMI onboard Sentinel-5 Precursor: algorithm theoretical basis, Atmos. Meas. Tech., 10(1), 119–153, doi:10.5194/amt-10-119-2017, 2017.
Theys, N., R. Volkamer, J.-F. Müller, K. J. Zarzana, N. Kille, L. Clarisse, I. De Smedt, C. Lerot, H. Finkenzeller, F. Hendrick, T. K. Koenig, C. F. Lee, C. Knote, H. Yu, and M. Van Roozendael: Global nitrous acid emissions and levels of regional oxidants enhanced by wildfires, *Nat. Geosci.*, ***13***, 681-686 (2020). https://doi.org/10.1038/s41561-020-0637-7

Theys, N., Fioletov, V., Li, C., De Smedt, I., Lerot, C., McLinden, C., Krotkov, N., Griffin, D., Clarisse, L., Hedelt, P., Loyola, D., Wagner, T., Kumar, V., Innes, A., Ribas, R., Hendrick, F., Vlietinck, J., Brenot, H., and Van Roozendael, M.: A sulfur dioxide Covariance-Based Retrieval Algorithm (COBRA): application to TROPOMI reveals new emission sources, Atmos. Chem. Phys., 21, 16727–16744, https://doi.org/10.5194/acp-21-16727-2021, 2021.

Van Damme, M., Clarisse, L., Franco, B., Sutton, M. A., Erisman, J. W., Kruit, R. W., van Zanten, M., Whitburn, S., Hadji-Lazaro, J., Hurtmans, D., Clerbaux, C., and Coheur, P.-F.: Global, regional and national trends of atmospheric ammonia derived from a decadal (2008-2018) satellite record. *Environ. Res. Lett.* **16(5)**, 055017 (2021). https://doi.org/10.1088/1748-9326/abd5e0

Van Damme, M., Clarisse, L., Whitburn, S., Hadji-Lazaro, J., Hurtmans, D., Clerbaux, C., and Coheur, P.-F.: Industrial and agricultural ammonia point sources exposed. *Nature* **564(7734)**, 99-103 (2018). https://doi.org/10.1038/s41586-018-0747-1

Van Damme, M., Whitburn, S., Clarisse, L., Clerbaux, C., Hurtmans, D., and Coheur, P.-F.: Version 2 of the IASI NH_3 neural network retrieval algorithm: near-real-time

and reanalysed datasets. *Atmos. Meas. Tech.* **10**, 4905-4914 (2017). https://doi.org/10.5194/amt-10-4905-2017

Vandaele, A. C. et al. Measurements of the NO2 absorption cross section from 42 000cm−1 to 10 000cm−1 (238–1000 nm) at 220K and 294 K. *J. Quant. Spectrosc. Ra.* **59**, 171–184 (1998).

Veefkind, J. P., Aben, I., McMullan, K., Förster, H., de Vries, J., Otter, G., Claas, J., Eskes, H. J., de Haan, J. F., Kleipool, Q., van Weele, M., Hasekamp, O., Hoogeven, R., Landgraf, J., Snel, R., Tol, P., Ingmann, P., Voors, R., Kruizinga, B., Vink, R., Visser, H., and Levelt, P. F.: TROPOMI on the ESA Sentinel-5 Precursor: A GMES mission for global observations of the atmospheric composition for climate, air quality and ozone layer applications, Remote Sens. Environ., 120, 70–83, doi:10.1016/j.rse.2011.09.027, 2012.

Walker, J. C., Dudhia, A., and Carboni, E.: An effective method for the detection of trace species demonstrated using the MetOp Infrared Atmospheric Sounding Interferometer, Atmos. Meas. Tech., 4, 1567–1580, https://doi.org/10.5194/amt-4-1567-2011, 2011.

Wang, P., Tuinder, O. N. E., Tilstra, L.G., de Graaf, M., Stammes, P. Interpretation of FRESCO cloud retrievals in case of absorbing aerosol events. *Atmos. Chem. Phys.* **12**, 9057-9077 (2012).

Whitburn, S., Clarisse, L., Crapeau, M., August, T., Hultberg, T., Coheur, P. F., and Clerbaux, C.: A CO_2-independent cloud mask from Infrared Atmospheric Sounding Interferometer (IASI) radiances for climate applications. *Atmos. Meas. Tech.* **15(22)**, 6653-6668 (2022). https://doi.org/10.5194/amt-15-6653-2022

Whitburn, S., Van Damme, M., Clarisse, L., Bauduin, S., Heald, C. L., Hadji-Lazaro, J., Hurtmans, D., Zondlo, M. A., Clerbaux, C., and Coheur, P.-F.: A flexible and robust neural network IASI-NH_3 retrieval algorithm. *J. Geophys. Res. Atmos.* **121(11)**, 6581–6599 (2016). https://doi.org/10.1002/2016JD024828

Winker, D. M., Vaughan, M. A., Omar, A., Hu, Y., Powell, K. A., Liu, Z., Hunt, W. H., and Young, S. A.: Overview of the CALIPSO Mission and CALIOP Data Processing Algorithms. *J. Atmos. Ocean. Technol.* **26(11)**, 2310-2323 (2009). https://doi.org/10.1175/2009JTECHA1281.1

Zhou, D., Larar, A., Liu, X., Smith, W., Strow, L., Yang, P., Schlüssel, P., and Calbet, X.: Global land surface emissivity retrieved from satellite ultraspectral IR measurements. *IEEE Trans. Geosci. Remote.* **49**, 1277-1290 (2011). https://doi.org/10.1109/TGRS.2010.2051036